ACS APPLIED MATERIALS & INTERFACES

www.acsami.org Research Article

Novel Quasi-2D Perovskites for Stable and Efficient Perovskite Solar Cells

Tao Zhu, Yongrui Yang, Kai Gu, Chunming Liu, Jie Zheng, and Xiong Gong*

Cite This: ACS Appl. Mater. Interfaces 2020, 12, 51744–51755 Read Online

ACCESS | Metrics & More | Article Recommendations | Supporting Information

ABSTRACT: Compared to three-dimensional (3D) organic−inorganic hybrid perovskites, two-dimensional (2D) ones possess great possibilities to realize stable cost-effective perovskite solar cells (PSCs). However, studies indicated that PSCs with 2D perovskites exhibited poor power conversion efficiencies (PCEs). In this study, we report novel propargylamine cation (PPA^+)-based quasi-2D perovskites. PPA^+ employed as an organic spacer is for enhancing charge-carrier transport of quasi-2D $(PPA)_2(CH_3NH_3)_2Pb_3I_{10}$ thin films, consequently boosting PCEs of PSCs. To further boost PCEs of PSCs with quasi-2D $(PPA)_2(CH_3NH_3)_2Pb_3I_{10}$ thin films, a quasi-2D $(PPA)_2(CH_3NH_3)_2Pb_3I_{10}$ thin film is processed with $Pb(SCN)_2$ additives. Systematical studies indicate that the quasi-2D $(PPA)_2(CH_3NH_3)_2Pb_3I_{10}$ thin film processed with $Pb(SCN)_2$ additives exhibits superior film morphology and crystallinity, larger crystals, reduced nonradiative charge-carrier recombination, and enhanced and balanced charge-carrier mobilities compared to the pristine quasi-2D $(PPA)_2(CH_3NH_3)_2Pb_3I_{10}$ thin film. As a result, PSCs with the quasi-2D $(PPA)_2(CH_3NH_3)_2Pb_3I_{10}$ thin film processed with $Pb(SCN)_2$ additives exhibit a PCE of 15.20%, which is an over 25% enhancement compared to those (12.16%) with a pristine quasi-2D $(PPA)_2(CH_3NH_3)_2Pb_3I_{10}$ thin film. In addition, PSCs with the quasi-2D $(PPA)_2(CH_3NH_3)_2Pb_3I_{10}$ thin film processed with $Pb(SCN)_2$ additives possess dramatically suppressed photocurrent hysteresis and significantly boosted stability. All these results indicate that we have developed a facile way to synthesize novel 2D perovskite thin films for realizing stable and efficient PSCs with dramatically suppressed photocurrent hysteresis.

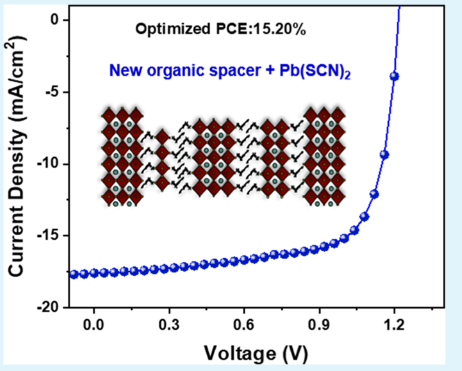

KEYWORDS: *perovskite solar cells, 2D perovskite materials, propargylamine organic spacer, $Pb(SCN)_2$ process additives, efficiency and stability*

■ INTRODUCTION

Organic−inorganic hybrid perovskites with a general chemical formula of ABX_3, where A is methylammonium (MA^+), formamidinium (FA^+), or Cs^+; B is Pb^{2+} or Sn^{2+}; and X is Cl^-, Br^-, or I^- or their combination, have drawn the greatest attention in both academic and industrial sectors because of their superior optoelectronic and photovoltaic properties.[1−6] Over 25% power conversion efficiencies (PCEs) have been reported from perovskite solar cells (PSCs) with three-dimensional (3D) perovskites.[7] Despite all of the astonishing progress made in the past decade, the intrinsic environmental instability issue of 3D perovskites needs to be addressed for further development and commercialization of PSCs.[8] There exist prior reports of two-dimensional (2D) layered perovskites, crafted using organic cations, for example, butylammonium (BA^+) and phenethylammonium (PEA^+), substituting either MA^+ or FA^+, that exhibited environmental stability, but possessed poor photovoltaic properties.[9−15] PCEs of 8.13 and 9.66% were reported for PSCs with either BA^+- or PEA^+-based 2D perovskites with lower *n* values (where *n* is the stacking number of the $[BX_6]$ network layers between two organic barrier layers),[9−15] respectively. Such low PCEs were ascribed to poor charge-carrier transport of BA^+- or PEA^+-based 2D perovskites.[14−16] Thus, the development of efficient organic spacers and understanding the charge transport mechanism are very important to further boost PCEs of PSCs. Recently, a PCE of 17.39% was reported for PSCs through alternating the ordering of diammonium (BEA^{2+}) and monoammonium (MA^+) cations in the interlayer space to form low-dimensional perovskites.[17] Xu et al.[18] reported two multiple-ring spacer cations, 1-naphthalenemethylammonium and 9-anthracenemethylammonium organic spacers, and further reported a PCE of 17.25% ($n = 4$) from PSCs. More recently, a PCE of 19.06% ($n = 5$) was further reported for PSCs with a 2D perovskite processed with an organic salt 4-(trifluoromethyl)-benzylammonium iodide.[19] Nevertheless, a PCE of >15% for PSCs with 2D perovskites with $n < 4$ was rarely reported.[20]

Received: September 13, 2020
Accepted: October 28, 2020
Published: November 4, 2020

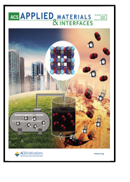

https://dx.doi.org/10.1021/acsami.0c16514
ACS Appl. Mater. Interfaces 2020, 12, 51744−51755

Scheme 1. (a) Schematic Illustrations of the PPA^+ Cation (Gray, Green, and Red Balls Represent C, H, and N Atoms, Respectively) and Realignment of the Quasi-2D Perovskite Crystal: (b) Pristine (Gray, Green, Light Green, and Yellow Balls Represent C, H, Atoms, and MA^+ and I^-, Respectively) and (c) Processed with $Pb(SCN)_2$ Additives

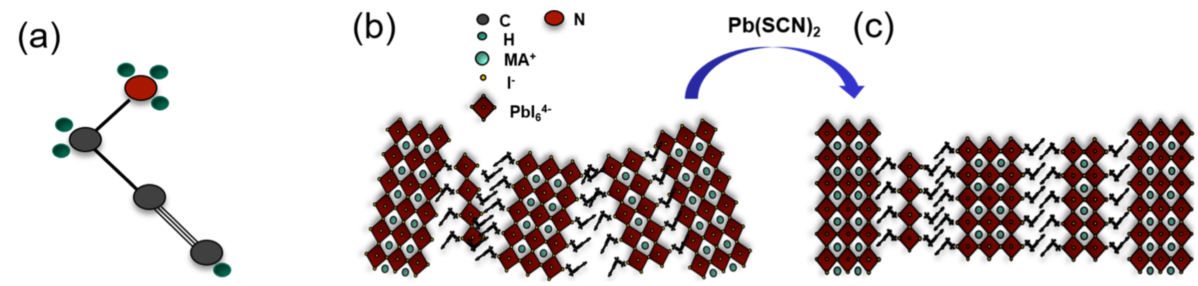

In this study, we report novel propargylamine (PPA^+)-based quasi-2D perovskites, where propargylamine (PPA^+), a new organic spacer cation, is employed to prepare a quasi-2D $(PPA)_2(CH_3NH_3)_2Pb_3I_{10}$ thin film for enhancing its charge-carrier transport, consequently boosting PCEs of PSCs. To further enhance the crystallinities of the quasi-2D $(PPA)_2(MA)_2Pb_3I_{10}$ thin film, a quasi-2D $(PPA)_2(MA)_2Pb_3I_{10}$ thin film is processed with $Pb(SCN)_2$ additives. Systematical studies indicate that the quasi-2D $(PPA)_2(MA)_2Pb_3I_{10}$ thin film processed with $Pb(SCN)_2$ additives possesses higher crystallinity, larger crystals, superior film morphology, reduced nonradiative recombination, and enhanced and balanced charge-carrier mobilities. As a result, the PSC with the quasi-2D $(PPA)_2(MA)_2Pb_3I_{10}$ thin film processed with $Pb(SCN)_2$ additives exhibits a PCE of 15.20%, which is an over 25% enhancement compared with that (12.16%) with the pristine quasi-2D $(PPA)_2(MA)_2Pb_3I_{10}$ thin film. Moreover, PSCs with the quasi-2D $(PPA)_2(MA)_2Pb_3I_{10}$ thin film processed with $Pb(SCN)_2$ additives exhibit dramatically boosted stability and suppressed photocurrent hysteresis.

EXPERIMENTAL SECTION

Materials. Propargylamine hydrochloride (PPA·HCl), lead(II) thiocyanate ($Pb(SCN)_2$), molybdenum(VI) oxide (99.97%), poly-[bis(4-phenyl)(2,4,6-trimethylphenyl)amine] (PTAA), dimethylformamide (DMF, anhydrous, 99.8%), dimethyl sulfoxide (DMSO, anhydrous, 99.9%), toluene (anhydrous, 99.8%), and aluminum slug were purchased from Sigma-Aldrich. Poly(3,4-ethylenedioxythiophene)polystyrene sulfonate (PEDOT:PSS) (SCA 388-20) was purchased from Heraeus. Lead iodide (PbI_2, 99.9985% metals basis) and tin oxide (15% in water colloidal dispersion) were purchased from Alfa Aesar. C_{60} (99.95% carbon powder) was purchased from Purec60oliveoil. Methyl-ammonium iodide (MAI) was purchased from Greatcell Solar. All materials are used as received without any further treatment.

Preparation of Precursor Solutions. The quasi-2D perovskite precursor solution was prepared by mixing of $Pb(SCN)_2$, PPA·HCl, MAI, and PbI_2 with a stoichiometric ratio of x:2:2:3 (where x is the $Pb(SCN)_2$ content) into 1 M DMF/DMSO (volume ratio of 4:1) solution. The perovskite precursor solution for making the 3D $CH_3NH_3PbI_3$ thin film was prepared in a stoichiometric ratio of 1:1 for MAI and PbI_2 into 1 M DMF/DMSO (volume ratio of 4:1) solution. All perovskite precursor solutions were thoroughly mixed and aged for 12 h before use.

Preparation of Quasi-2D and 3D Perovskite Thin Films. Precleaned quartz (or glass) substrates were treated with UV−ozone plasma for about 20 min. The quasi-2D $(PPA)_2(MA)_2Pb_3I_{10}$ and 3D $CH_3NH_3PbI_3$ thin films were prepared by a one-step method with a spin speed of 4000 rpm for 30 s. To make a homogenous thin film, the dropped perovskite precursor solutions should completely cover the surface of substrates. After that, thin films were thermally annealed at 100 °C for 10 min and then cooled down to room temperature naturally.

Characterization of Perovskite Thin Films. The X-ray diffraction (XRD) patterns were obtained by Rigaku SmartLab XRD. The absorption spectra were characterized using a Lambda 900 UV−vis−NIR spectrophotometer (PerkinElmer, Waltham, MA, USA). The photoluminescence (PL) spectra were obtained using a QuantaMaster 2361 (HORIBA). Scanning electron microscopy (SEM) images were obtained using field-emission SEM (model JEOL-7401). The thicknesses were measured using a Bruker DektakXT Stylus profilometer with a scan rate of 0.03 mm s^{-1}. Grazing-incidence wide-angle X-ray scattering (GIWAXS) was performed on the dedicated high-resolution GIWAXS beamline (Sector 8-ID-E) in the Advanced Photon Source, Argonne National Laboratory, at an incident angle of 0.14°. The GIWAXS data were collected by exposing the samples to X-rays for 10 s, and the collected data were analyzed using MATLAB-based software (GIXSGUI). Individual 3D $MAPbI_3$ thin films, quasi-2D $(PPA)_2(MA)_2Pb_3I_{10}$ thin films, and the quasi-2D $(PPA)_2(MA)_2Pb_3I_{10}$ thin film processed with 3% $Pb(SCN)_2$ additives were imaged using total internal reflection fluorescence microscopy (TIRFM) under a wavelength of 532 nm laser excitation. The excitation laser intensities were 0.25 mW. The PL of perovskite particles was filtered using a 542 nm long-pass filter and a 585/65 nm single bandpass filter and collected using a sCMOS camera. Under each experimental condition, 1000 consecutive images of perovskite particles were taken with the exposure time set to 10 ms.

Fabrication of PSCs with Quasi-2D $(PPA)_2(MA)_2Pb_3I_{10}$ Thin Films. Precleaned ITO/glass substrates were treated with UV−ozone plasma for about 20 min, where ITO is indium tin oxide. Then, a ∼20 nm PTAA thin film was spin-cast on the top of ITO/glass substrates with a spin speed of 6000 rpm for 30 s from 2 mg/mL PTAA toluene solution, followed by thermal annealing at 100 °C for 10 min. After the PTAA-coated substrates were cooled down to room temperature, the quasi-2D $(PPA)_2(MA)_2Pb_3I_{10}$ thin film was prepared by a one-step method as described above. Afterward, ∼40 nm C_{60} was thermally deposited on the top of the quasi-2D $(PPA)_2(MA)_2Pb_3I_{10}$ thin film in a vacuum system with a base pressure of 10^{-6} Torr. PSCs were completed by thermal deposition of ∼100 nm Al on the top of the C_{60} layer in a vacuum system. The device area was measured to be 0.045 cm^2.

Characterization of PSCs. The current densities versus voltages ($J-V$) characteristics of PSCs were tested using a Keithley model 2400 source measure unit. The light source was a Newport Air Mass 1.5 Global (AM1.5G) full-spectrum simulator with a light intensity of 100 mW·cm^{-2}, which was calibrated by utilizing a monosilicon detector (with a KG-5 visible color filter) from the National Renewable Energy Laboratory to reduce the spectral mismatch. The external quantum efficiency (EQE) spectrum was obtained on a solar cell quantum efficiency measurement system (QEX10). Impedance spectroscopy (IS) was conducted using an HP 4194A impedance/gain-phase analyzer under illumination and in the dark, at the voltage closing to a V_{OC} condition. The frequency is varied from 5 to 105 Hz. Both capacitance−voltage ($C-V$) and capacitance−frequency ($C-F$) testing were also performed using the same setup. The transient

https://dx.doi.org/10.1021/acsami.0c16514
ACS Appl. Mater. Interfaces 2020, 12, 51744−51755

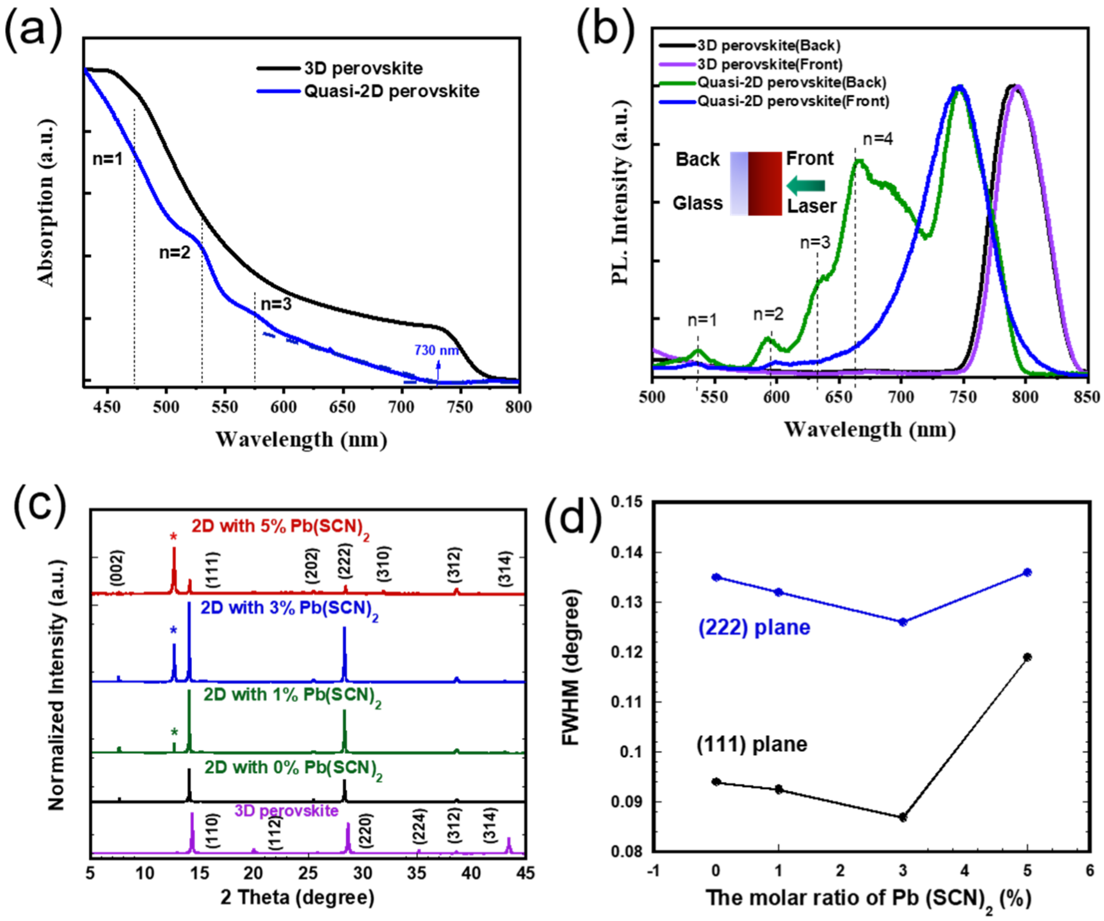

Figure 1. (a) Absorption spectra of the 3D $MAPbI_3$ thin film and quasi-2D $(PPA)_2(MA)_2Pb_3I_{10}$ thin film and (b) PL spectra of the 3D $MAPbI_3$ thin film and quasi-2D $(PPA)_2(MA)_2Pb_3I_{10}$ thin film measured from the back and front side, excited at a wavelength of 420 nm. (c) XRD patterns of the 3D $MAPbI_3$ thin film, pristine quasi-2D $(PPA)_2(MA)_2Pb_3I_{10}$ thin film, and quasi-2D $(PPA)_2(MA)_2Pb_3I_{10}$ thin films processed with $Pb(SCN)_2$ additives. The star indicates the impurities of PbI_2. (d) fwhms for the (111) and (222) planes from the quasi-2D $(PPA)_2(MA)_2Pb_3I_{10}$ thin films processed with $Pb(SCN)_2$ additives.

photocurrent (TPC) measurement was done using a homemade setup in our laboratory.[8,21,22]

RESULTS AND DISCUSSION

The molecular structures of the PPA^+ cation and the corresponding quasi-2D $(PPA)_2(MA)_2Pb_3I_{10}$ perovskites are schematically displayed in Schemes 1a,b. The nominal *n*-value (3) in this work is estimated based on the stoichiometry of precursors. PPA^+ is employed as an organic spacer to form 2D perovskite thin films because the carbon−carbon triple bond (C≡C) in the PPA^+ molecule could prevent intramolecular hydrogen bonds and decrease the alkalinity and nucleophilicity of $-NH_2$. Moreover, PPA^+ has a shorter chain length than that of either BA^+ or PEA^+.[9−15] Such a short-chain length could facilitate charge carriers to be efficiently transported within $(PPA)_2(MA)_2Pb_3I_{10}$ thin films, resulting in boosted charge-carrier transport within $(PPA)_2(MA)_2Pb_3I_{10}$ thin films.[14−16] As a result, high short circuit photocurrent (J_{SC}) is anticipated to be observed from PSCs with $(PPA)_2(MA)_2Pb_3I_{10}$ thin films.

Figure 1a displays the absorption spectra of the $(PPA)_2(MA)_2Pb_3I_{10}$ thin film and 3D $MAPbI_3$ thin film casted on the quartz substrates. Based on the absorption spectrum, the optical bandgap of the $(PPA)_2(MA)_2Pb_3I_{10}$ thin film is calculated to be 1.70 eV, which is larger than that (1.59 eV) for the 3D $MAPbI_3$ thin film. It is clear that the absorption spectrum of the $(PPA)_2(MA)_2Pb_3I_{10}$ thin film is different to that of the 3D $MAPbI_3$ thin film. Moreover, the characteristic exciton peaks of the $(PPA)_2(MA)_2Pb_3I_{10}$ thin film for $n = 1$, 2, and 3 are located at 471, 529, and 575 nm, respectively, which indicates that strong quantum confinement takes place in the $(PPA)_2(MA)_2Pb_3I_{10}$ thin film.

Figure 1b presents the PL spectra of $(PPA)_2(MA)_2Pb_3I_{10}$ and 3D $MAPbI_3$ thin films casted on the glass substrates, measured from both the front (air) side and the back (glass) side, under the same monochromatic light excitation at a wavelength of 420 nm. The PL spectrum of the 3D $MAPbI_3$ thin film measured from the back side is nearly identical to that measured from the front side. However, the PL spectrum of the $(PPA)_2(MA)_2Pb_3I_{10}$ thin film measured from the front side is dramatically different to that from the back side, which indicates that multiple perovskite phases (n) coexist within the $(PPA)_2(MA)_2Pb_3I_{10}$ thin film.[14−16] Moreover, compared with the PL spectrum of the $(PPA)_2(MA)_2Pb_3I_{10}$ thin film measured from the back side, the PL spectrum of the thin film measured from the front side exhibit four obvious intense peaks, which correspond to $n = 4$, 3, 2, and 1, respectively.[9,10] These significant differences demonstrate that the layered perovskite phases with smaller n is probably preferably formed at the bottom, while the perovskite phases with a larger n (3D phase) is probably preferably formed at the surface of the thin

https://dx.doi.org/10.1021/acsami.0c16514
ACS Appl. Mater. Interfaces 2020, 12, 51744−51755

film.[13] In addition, the blue-shifted PL spectrum observed from the $(PPA)_2(MA)_2Pb_3I_{10}$ thin film compared to that of the 3D $MAPbI_3$ thin film further confirms that strong quantum confinement takes place in the $(PPA)_2(MA)_2Pb_3I_{10}$ thin film.

In addition, the exciton binding energies of the 3D $MAPbI_3$ thin film and $(PPA)_2(MA)_2Pb_3I_{10}$ thin film are further estimated. The exciton binding energies are estimated by a difference between the optical energy gap and the exciton energy gap, $\Delta E = E_{opt} - E_{ex}$,[23] where E_{opt} is the optical energy gap and E_{ex} is the exciton energy gap. Based on the absorption cut-off and PL peak, the exciton binding energy of the 3D $MAPbI_3$ thin film is estimated to be 30 meV; whereas the exciton binding energies of the $(PPA)_2(MA)_2Pb_3I_{10}$ thin film are estimated to be 320, 260, 190, and 50 meV, for n = 1, 2, 3, and ∞, respectively. Thus, it is concluded that the $(PPA)_2(MA)_2Pb_3I_{10}$ thin film is with a quasi-2D structure rather than with a pure 2D structure.[10] The optoelectronic properties of 3D $MAPbI_3$ and quasi-2D $(PPA)_2(MA)_2Pb_3I_{10}$ thin films are summarized in Table 1.

Table 1. Optoelectronic Properties of 3D $MAPbI_3$ and Quasi-2D $(PPA)_2(MA)_2Pb_3I_{10}$ Thin Films

perovskite thin films	optical band gap (eV)	exciton energy (eV)	exciton binding energy (meV)
quasi-2D (n = 1) phase	2.63	2.31	320
quasi-2D (n = 2) phase	2.34	2.08	260
quasi-2D (n = 3) phase	2.15	1.96	190
quasi-2D (n = ∞) phase	1.70	1.65	50
3D perovskite	1.59	1.56	30

Figure 1c shows the XRD patterns of the 3D $MAPbI_3$ thin film and quasi-2D $(PPA)_2(MA)_2Pb_3I_{10}$ thin films casted on glass substrates. The (110), (112), (220), (224), (312), and (314) planes observed from the 3D $MAPbI_3$ thin film and the (111), (202), (222), (310), (312), and (314) planes observed from the quasi-2D $(PPA)_2(MA)_2Pb_3I_{10}$ thin film demonstrate that both of them possess a typical tetragonal structure.[4] However, the quasi-2D $(PPA)_2(MA)_2Pb_3I_{10}$ thin film possesses a peak located at a 2θ of ~7°, corresponding to the (002) plane, which is the characteristic feature of 2D perovskites.[9] These results further confirm that the $(PPA)_2(MA)_2Pb_3I_{10}$ thin film possesses a quasi-2D structure.[17−20]

To further enhance the crystallinities of quasi-2D $(PPA)_2(MA)_2Pb_3I_{10}$ thin films, quasi-2D $(PPA)_2(MA)_2Pb_3I_{10}$ thin films are processed from their corresponding precursor solutions mixed with $Pb(SCN)_2$ additives. $Pb(SCN)_2$ is selected as the processing additives because it is a Lewis base, which could interact with under-coordinated Pb atoms and halide vacancies as well, tuning the perovskite crystal growing processes. Note that the excess SCN^- would form HSCN gas to be finally removed from quasi-2D $(PPA)_2(MA)_2Pb_3I_{10}$ thin films during the thermal annealing process because HSCN possesses a low boiling point (−87.78 °C).[24,25] A schematic illustration of perovskite crystal growth processes tuned by $Pb(SCN)_2$ additives is proposed in Scheme 1b,c. Thus, the quasi-2D $(PPA)_2(MA)_2Pb_3I_{10}$ thin films processed with $Pb(SCN)_2$ additives are expected to possess better crystallinity.

To verify the abovementioned hypothesis, XRD is carried out to study the crystal structure of the quasi-2D $(PPA)_2(MA)_2Pb_3I_{10}$ thin films processed with $Pb(SCN)_2$ additives and the results are also shown in Figure 1c. The quasi-2D $(PPA)_2(MA)_2Pb_3I_{10}$ thin films processed with $Pb(SCN)_2$ additives possess the same lattice planes as the pristine quasi-2D $(PPA)_2(MA)_2Pb_3I_{10}$ thin film does. In addition, a refraction peak corresponding to PbI_2 crystals is presented within the quasi-2D $(PPA)_2(MA)_2Pb_3I_{10}$ thin films processed with $Pb(SCN)_2$ additives, and the peak intensities increased with increasing concentrations of $Pb(SCN)_2$ additives. These results indicate that extra Pb^{2+} from $Pb(SCN)_2$ additives interacts with I^-, forming PbI_2 crystals.

Moreover, it is found that the peak intensities of the lattice planes for the quasi-2D $(PPA)_2(MA)_2Pb_3I_{10}$ thin films processed with $Pb(SCN)_2$ additives increased and then decreased with increasing concentrations of $Pb(SCN)_2$ additives. The full width at half-maximums (fwhms) of the (111) and (222) planes for the quasi-2D $(PPA)_2(MA)_2Pb_3I_{10}$ thin films processed with $Pb(SCN)_2$ additives are calculated and the results are shown in Figure 1d. Both fwhm values of

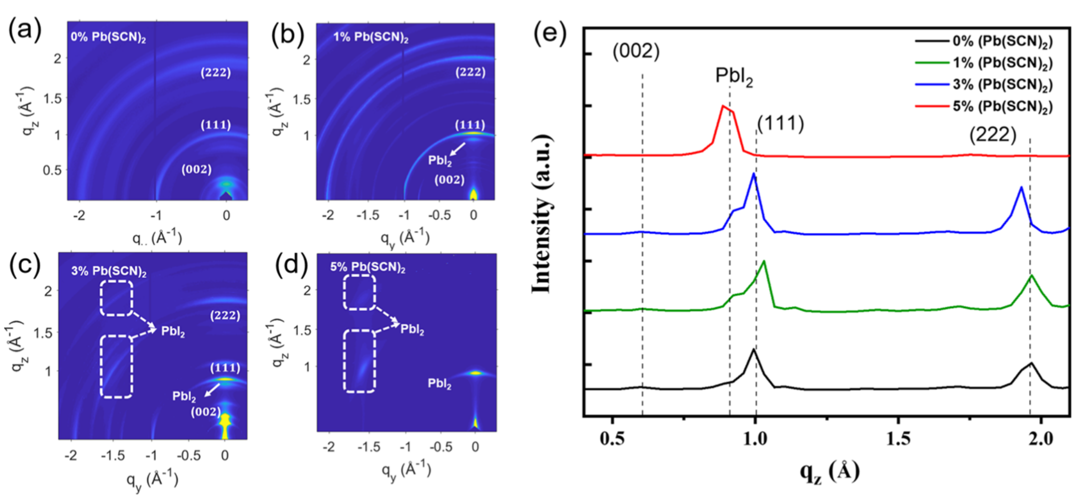

Figure 2. 2D GIWAXS profiles of (a) pristine quasi-2D $(PPA)_2(MA)_2Pb_3I_{10}$ thin film and quasi-2D $(PPA)_2(MA)_2Pb_3I_{10}$ thin films processed with (b) 1% $Pb(SCN)_2$, (c) 3% $Pb(SCN)_2$, and (d) 5% $Pb(SCN)_2$ additives and (e) 1D GIWAXS line profiles extracted from (a−d) (out-of-plane direction, incident angle of 0.14°).

https://dx.doi.org/10.1021/acsami.0c16514
ACS Appl. Mater. Interfaces 2020, 12, 51744−51755

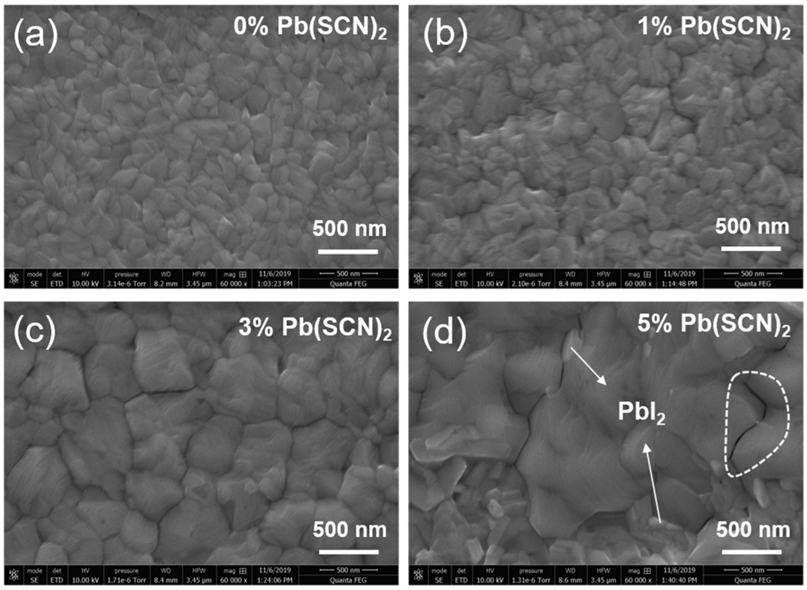

Figure 3. SEM images of (a) pristine quasi-2D $(PPA)_2(MA)_2Pb_3I_{10}$ thin film and quasi-2D $(PPA)_2(MA)_2Pb_3I_{10}$ thin films processed with (b) 1% $Pb(SCN)_2$, (c) 3% $Pb(SCN)_2$, and (d) 5% $Pb(SCN)_2$ additives, respectively.

the (111) and the (222) planes decreased for the quasi-2D $(PPA)_2(MA)_2Pb_3I_{10}$ thin films processed with either 1 or 3% of $Pb(SCN)_2$ additives and then increased with 5% of $Pb(SCN)_2$ additives. The decreased fwhm values indicate that the quasi-2D $(PPA)_2(MA)_2Pb_3I_{10}$ thin films processed with low concentrations of $Pb(SCN)_2$ additives possess an optimal crystallinity with few crystal imperfections and structural defects, and the increased fwhm value indicates that the quasi-2D $(PPA)_2(MA)_2Pb_3I_{10}$ thin film processed with high concentrations of $Pb(SCN)_2$ additives exhibits poor crystallinity.[26] Thus, the XRD results confirm that $Pb(SCN)_2$ processing additives could effectively tune the crystalline features, resulting in high-quality quasi-2D $(PPA)_2(MA)_2Pb_3I_{10}$ thin films as the concentration of $Pb(SCN)_2$ additives is lower than 5%.

Figure 2a−d displays the orientation of the quasi-2D $(PPA)_2(MA)_2Pb_3I_{10}$ thin films processed with $Pb(SCN)_2$ additives investigated by GIWAXS. The quasi-2D $(PPA)_2(MA)_2Pb_3I_{10}$ thin films show randomly oriented features for the (111) and (222) planes (Figure 2a). Clearly visible spots in the ring with oriented crystals are observed from the quasi-2D $(PPA)_2(MA)_2Pb_3I_{10}$ thin films processed with both 1% and 3% $Pb(SCN)_2$ additives (Figure 2b,c), which indicates that these crystals are oriented.[6,26] However, the PbI_2 impurity peak is visible within the quasi-2D $(PPA)_2(MA)_2Pb_3I_{10}$ thin films processed with 3% $Pb(SCN)_2$ additives. Moreover, the PbI_2 impurity peak are obviously observed from the quasi-2D $(PPA)_2(MA)_2Pb_3I_{10}$ thin film processed with 5% $Pb(SCN)_2$ additives (Figure 2d), which indicates that there is quite an amount of PbI_2 clusters within quasi-2D $(PPA)_2(MA)_2Pb_3I_{10}$ thin films.

Figure 2e shows the 1D GIWAXS line profiles of the pristine quasi-2D $(PPA)_2(MA)_2Pb_3I_{10}$ thin film and the quasi-2D $(PPA)_2(MA)_2Pb_3I_{10}$ thin films processed with $Pb(SCN)_2$ additives, which are extracted from the out-of-plane directions of 2D GIWAXS. The increased intensities of the (111) and the (222) peaks observed from the quasi-2D $(PPA)_2(MA)_2Pb_3I_{10}$ thin films processed with both 1 and 3% $Pb(SCN)_2$ additives indicate that the (111) and (222) planes are more oriented in these quasi-2D $(PPA)_2(MA)_2Pb_3I_{10}$ thin films. However, both the (111) and (222) planes disappeared in the quasi-2D $(PPA)_2(MA)_2Pb_3I_{10}$ thin film processed with 5% $Pb(SCN)_2$ additives. This is probably ascribed to the fact that these disappeared planes are overaged by the excess of PbI_2 clusters at the surface of the resultant quasi-2D $(PPA)_2(MA)_2Pb_3I_{10}$ thin film. The lattice planes corresponding to the PbI_2 clusters are nearby the (111) plane, and the strong refraction from the PbI_2 clusters probably covers the (111) plane.

Figure 3 displays the top-view SEM images of quasi-2D $(PPA)_2(MA)_2Pb_3I_{10}$ thin films casted on the PTAA/ITO/glass substrates. A smooth and full-coverage film with densely packed crystalline grains and ∼100 nm crystal size is observed for pristine quasi-2D $(PPA)_2(MA)_2Pb_3I_{10}$ thin film. The quasi-2D $(PPA)_2(MA)_2Pb_3I_{10}$ thin film processed with 1% $Pb(SCN)_2$ additives maintains the features as the pristine quasi-2D $(PPA)_2(MA)_2Pb_3I_{10}$ thin film does, but with dramatically enlarged crystal size (∼300 nm). Furthermore, the crystal grain sizes of the quasi-2D $(PPA)_2(MA)_2Pb_3I_{10}$ thin film processed with 3% $Pb(SCN)_2$ additives are enlarged to ∼500 nm. The quasi-2D $(PPA)_2(MA)_2Pb_3I_{10}$ thin film processed with 5% $Pb(SCN)_2$ additives exhibit even larger crystal sizes (over 700 nm), but with considerable amounts of voids and pinholes. All these results demonstrate that the $Pb(SCN)_2$ processing additives could effectively tune the crystallinities of quasi-2D $(PPA)_2(MA)_2Pb_3I_{10}$ thin films and promote the growth of large perovskite crystals.

In addition, as indicated in Figure 3d, small PbI_2 clusters are present in the quasi-2D $(PPA)_2(MA)_2Pb_3I_{10}$ thin film processed with 5% $Pb(SCN)_2$ additives, but such PbI_2 clusters are too small to be found in the quasi-2D $(PPA)_2(MA)_2Pb_3I_{10}$ thin film processed with 3% $Pb(SCN)_2$ additives. These PbI_2 clusters probably appear at the surface of the quasi-2D $(PPA)_2(MA)_2Pb_3I_{10}$ thin film processed with 5% $Pb(SCN)_2$ additives, whereas few smaller PbI_2 clusters are probably randomly well-distributed in the bulk of quasi-2D $(PPA)_2(MA)_2Pb_3I_{10}$ thin films processed with 3% $Pb(SCN)_2$.

TIRFM is further carried out to investigate PL profiles of individual perovskite particles.[27] Figure 4 presents the PL

https://dx.doi.org/10.1021/acsami.0c16514
ACS Appl. Mater. Interfaces 2020, 12, 51744−51755

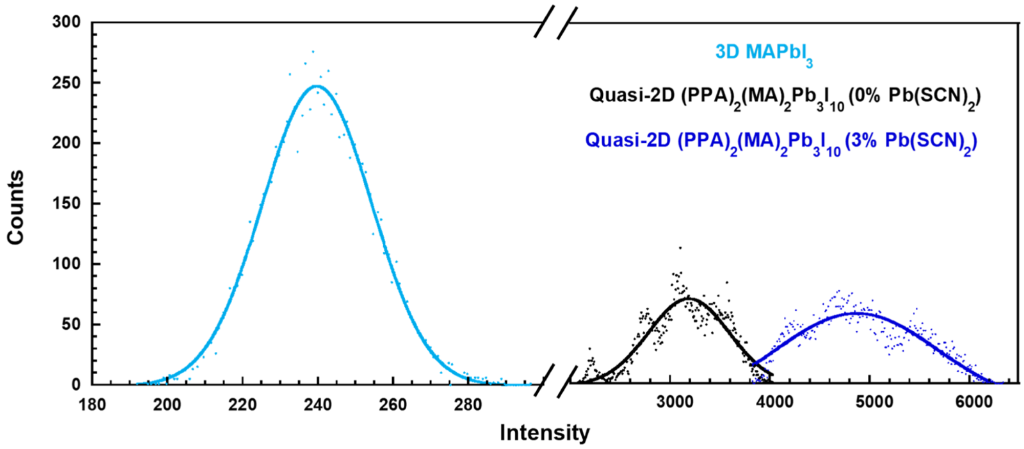

Figure 4. PL intensity histogram of TIRFM for individual perovskite particles of the 3D $MAPbI_3$ thin film, pristine quasi-2D $(PPA)_2(MA)_2Pb_3I_{10}$ thin film, and quasi-2D $(PPA)_2(MA)_2Pb_3I_{10}$ thin film processed with 3% $Pb(SCN)_2$ additives.

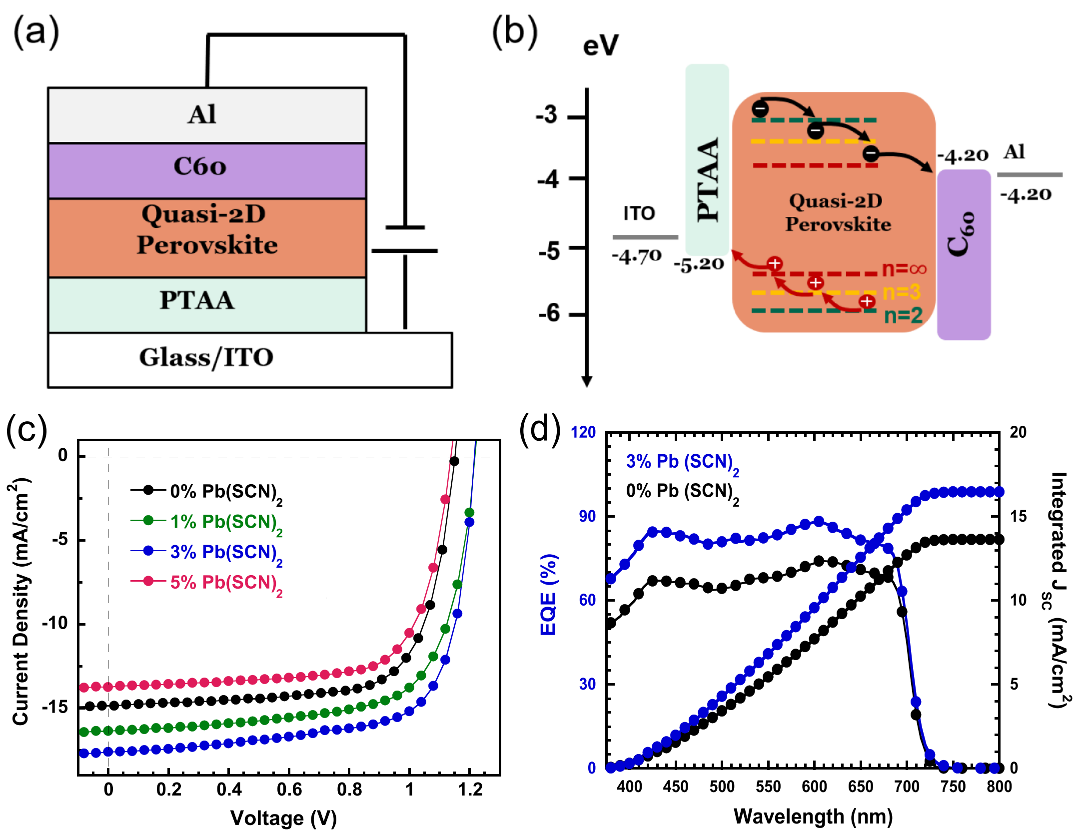

Figure 5. (a) Device structure of PSCs and (b) CBs and VBs of the quasi-2D $(PPA)_2(MA)_2Pb_3I_{10}$ thin film, the LUMO and HOMO energy levels of PTAA and C_{60}, and the work functions of ITO and Al. (c) *J*−*V* characteristics of PSCs with the quasi-2D $(PPA)_2(MA)_2Pb_3I_{10}$ thin film processed with $Pb(SCN)_2$ additives and (d) EQE spectra and the integrated photocurrent density of PSCs with either the pristine quasi-2D $(PPA)_2(MA)_2Pb_3I_{10}$ thin film or the quasi-2D $(PPA)_2(MA)_2Pb_3I_{10}$ thin film processed with 3% $Pb(SCN)_2$ additives.

intensity histogram of TIRFM for individual perovskite particles of the 3D $MAPbI_3$ thin film, the pristine quasi-2D $(PPA)_2(MA)_2Pb_3I_{10}$ thin film, and the quasi-2D $(PPA)_2(MA)_2Pb_3I_{10}$ thin film processed with 3% $Pb(SCN)_2$ additives, which can also be observed from TIRFM images shown in Supporting Information 1. Compared to the PL intensity of 3D $MAPbI_3$ perovskite particles (μ = 240, where μ is the mean of distribution), the enhancement in PL intensity for perovskite particles of quasi-2D $(PPA)_2(MA)_2Pb_3I_{10}$ (μ = 3188) indicates a much stronger exciton binding energy, which further confirms that the $(PPA)_2(MA)_2Pb_3I_{10}$ thin film is with a quasi-2D structure. In addition, it is clear that the quasi-2D $(PPA)_2(MA)_2Pb_3I_{10}$ thin film processed with 3% $Pb(SCN)_2$ additives (μ = 4872) exhibits more intense PL compared to the pristine quasi-2D $(PPA)_2(MA)_2Pb_3I_{10}$ thin film (μ = 3188). These observations demonstrate that the nonradiative recombination in the quasi-2D perovskite thin film processed with 3% $Pb(SCN)_2$ additives is dramatically suppressed. In addition, these observations are consistent with the SEM characteristics.

In order to verify that PPA^+ with a short-chain length could facilitate efficient charge-carrier transport, charge-carrier

https://dx.doi.org/10.1021/acsami.0c16514
ACS Appl. Mater. Interfaces 2020, 12, 51744−51755

mobility of quasi-2D $(PPA)_2(MA)_2Pb_3I_{10}$ thin films is investigated through a single-carrier device based on the space charge limited current (SCLC) method, according to the Mott−Gurney law.[28−31] The electron-only diode with a device structure of ITO/SnO_2/active layer/C_{60}/Al and the hole-only diode with a device structure of ITO/PEDOT:PSS/active layer/MoO_3/Ag, where the active layer is either the pristine quasi-2D $(PPA)_2(MA)_2Pb_3I_{10}$ thin film or the quasi-2D $(PPA)_2(MA)_2Pb_3I_{10}$ thin film processed with 3% $Pb(SCN)_2$ additives, respectively, are fabricated and characterized. As shown in Supporting Information 2, the $J-V$ characteristics can be divided into the Ohmic region ($J \propto V$) at low bias and the SCLC region ($J \propto V^2$) under high bias. The $J-V$ curve in the SCLC region can be well-fitted by the Mott−Gurney law[28−31]

$$J = \frac{9\varepsilon\varepsilon_0\mu V^2}{8L^3} \quad (1)$$

where μ is the charge-carrier mobility, V is the external bias, L is the thickness of the quasi-2D $(PPA)_2(MA)_2Pb_3I_{10}$ thin film, ε_0 is the vacuum permittivity, and ε is the dielectric constant for quasi-2D $(PPA)_2(MA)_2Pb_3I_{10}$, which is described by[28−31]

$$C = \varepsilon\varepsilon_0\frac{A}{d} \quad (2)$$

where A is the device area and d is the film thickness of the quasi-2D $(PPA)_2(MA)_2Pb_3I_{10}$ thin film. The capacitance versus frequency characteristics of photodiodes with a device structure of ITO/active layer (~350 nm)/Al, where the active layer is either the pristine quasi-2D $(PPA)_2(MA)_2Pb_3I_{10}$ thin film or the quasi-2D $(PPA)_2(MA)_2Pb_3I_{10}$ thin film processed with 3% $Pb(SCN)_2$ additives, are studied and characterized (Supporting Information 2). According to eq 2, the ε values are calculated to be 5.4 and 5.5 for the pristine quasi-2D $(PPA)_2(MA)_2Pb_3I_{10}$ thin film and the quasi-2D $(PPA)_2(MA)_2Pb_3I_{10}$ thin film processed with 3% $Pb(SCN)_2$ additives, respectively. Thus, based on eq 1, the electron and hole mobilities of pristine quasi-2D $(PPA)_2(MA)_2Pb_3I_{10}$ thin film are calculated to be 9.34×10^{-4} and 4.51×10^{-3} $cm^2\ V^{-1}\ s^{-1}$, respectively (μ_e/μ_h = 0.21). Both hole mobility and electron mobility of the pristine quasi-2D $(PPA)_2(MA)_2Pb_3I_{10}$ thin film are higher than the reported values (e.g., a hole mobility of 1.5×10^{-4} $cm^2\ V^{-1}\ s^{-1}$ and an electron mobility of $\sim 10^{-4}$ $cm^2\ V^{-1}\ s^{-1}$ for BA-based quasi-2D perovskites; a hole mobility of 2.8×10^{-5} $cm^2\ V^{-1}\ s^{-1}$ and an electron mobility of 2.5×10^{-3} $cm^2\ V^{-1}\ s^{-1}$ for PEA-based quasi-2D perovskites).[32,33] Such boosted charge-carrier mobilities are attributed to a shorter chain length of the organic spacer PPA^+ compared with that of either BA^+ or PEA^+ spacers. Moreover, the electron and hole mobilities of the quasi-2D $(PPA)_2(MA)_2Pb_3I_{10}$ thin film processed with 3% $Pb(SCN)_2$ additives are calculated to be 7.45×10^{-3} and 8.72×10^{-3} $cm^2\ V^{-1}\ s^{-1}$, respectively, which indicates that charge-carrier transport is tended to be balanced (μ_e/μ_h = 0.85). It is clear that the quasi-2D $(PPA)_2(MA)_2Pb_3I_{10}$ thin film processed with 3% $Pb(SCN)_2$ additives possesses both enhanced and balanced charge-carrier mobilities compared to the pristine quasi-2D $(PPA)_2(MA)_2Pb_3I_{10}$ thin film. Therefore, enhanced J_{SC} is expected to be observed for PSCs with the quasi-2D $(PPA)_2(MA)_2Pb_3I_{10}$ thin film processed with 3% $Pb(SCN)_2$ additives.

The photovoltaic properties of quasi-2D $(PPA)_2(MA)_2Pb_3I_{10}$ thin films are investigated through the characterization of PSCs with a device configuration of ITO/PTAA/quasi-2D $(PPA)_2(MA)_2Pb_3I_{10}$/C_{60}/Al, as shown in Figure 5a, where ITO acts as the anode, PTAA acts as the hole extraction layer (HEL), C_{60} is used as the electron extraction layer (EEL) and the hole blocking layer, and Al acts as the cathode, respectively. The highest occupied molecular orbit (HOMO) energy levels and the lowest unoccupied molecular orbit (LUMO) energy levels of PTAA and C_{60}, the conduction band (CB) and valence band (VB) of quasi-2D $(PPA)_2(MA)_2Pb_3I_{10}$, and the work functions of the ITO anode and the Al cathode are shown in Figure 5b. As indicated in Figure 1b, the layered perovskite phases with smaller n are preferably formed at the bottom, while those with larger n (3D phase) are preferably formed at the surface of the thin film, indicating that multiple energetic states coexist in quasi 2D perovskite thin films. Both CB and VB energy levels of the quasi-2D $(PPA)_2(MA)_2Pb_3I_{10}$ thin film from a low n value to a high n value exhibit a stepwise alignment, which indicates that the photogenerated electrons and holes could be effectively extracted from quasi-2D $(PPA)_2(MA)_2Pb_3I_{10}$ thin films. Moreover, a HOMO of −5.20 eV for the PTAA HEL and a LUMO of −4.20 eV for the C_{60} EEL are well-matched with perovskites with an n value of ∞ (3D perovskite), leading to effective extraction of charge carriers from the quasi-2D $(PPA)_2(MA)_2Pb_3I_{10}$ active layer to the ITO anode and the Al cathode. Thus, a boosted J_{SC} from PSCs is anticipated.

The $J-V$ characteristics of PSCs under AM1.5G illumination with a light intensity of 100 mW/cm^2, measured with a scan rate of 0.05 V s^{-1}, are shown in Figure 5c. The PSCs with the pristine quasi-2D $(PPA)_2(MA)_2Pb_3I_{10}$ thin film exhibit a J_{SC} of 14.84 $mA\cdot cm^{-2}$, an open circuit voltage (V_{OC}) of 1.15 V, a fill factor (FF) of 71%, and a corresponding PCE of 12.16%. These device performance parameters are higher than those for PSCs with BA- and/or PEA-based quasi-2D perovskites,[14,15] indicating that the carbon−carbon triple bond (C≡C) in the PPA^+ molecule could prevent the formation of intramolecular hydrogen bonds and decrease the alkalinity and nucleophilicity of $-NH_2$, resulting in enhanced charge-carrier mobilities, consequently, and boosted device performance of PSCs. The PSCs with the quasi-2D $(PPA)_2(MA)_2Pb_3I_{10}$ thin film processed with 1% $Pb(SCN)_2$ additives exhibit a J_{SC} of 16.35 $mA\cdot cm^{-2}$, a V_{OC} of 1.20 V, a FF of 70%, and a corresponding PCE of 13.78%. Moreover, the PSCs with the quasi-2D $(PPA)_2(MA)_2Pb_3I_{10}$ thin film processed with 3% $Pb(SCN)_2$ additives exhibit a J_{SC} of 17.60 $mA\cdot cm^{-2}$, a V_{OC} of 1.20 V, a FF of 72%, and a corresponding PCE of 15.20%, which is a 25% enhancement compared with that (12.16%) for the pristine quasi-2D $(PPA)_2(MA)_2Pb_3I_{10}$ thin film. Dramatically enhanced device performance is ascribed to higher crystallinity of the quasi-2D $(PPA)_2(MA)_2Pb_3I_{10}$ thin films processed with $Pb(SCN)_2$ additives. However, the PSCs with the quasi-2D $(PPA)_2(MA)_2Pb_3I_{10}$ thin film processed with 5% $Pb(SCN)_2$ additives exhibit a J_{SC} of 13.77 $mA\cdot cm^{-2}$, a V_{OC} of 1.12 V, a FF of 72%, and a corresponding PCE of 11.14%. Such a poor device performance is probably attributed to the excess amounts of voids and pinholes on the surface of the thin film (Figure 3d), leading to serious surface charge-carrier recombination, consequently resulting in poor device performance. In addition, excess of PbI_2 is also detrimental to device performance.[34] All these results are well consistent with the XRD analysis and SEM characterizations discussed above.

https://dx.doi.org/10.1021/acsami.0c16514
ACS Appl. Mater. Interfaces 2020, 12, 51744−51755

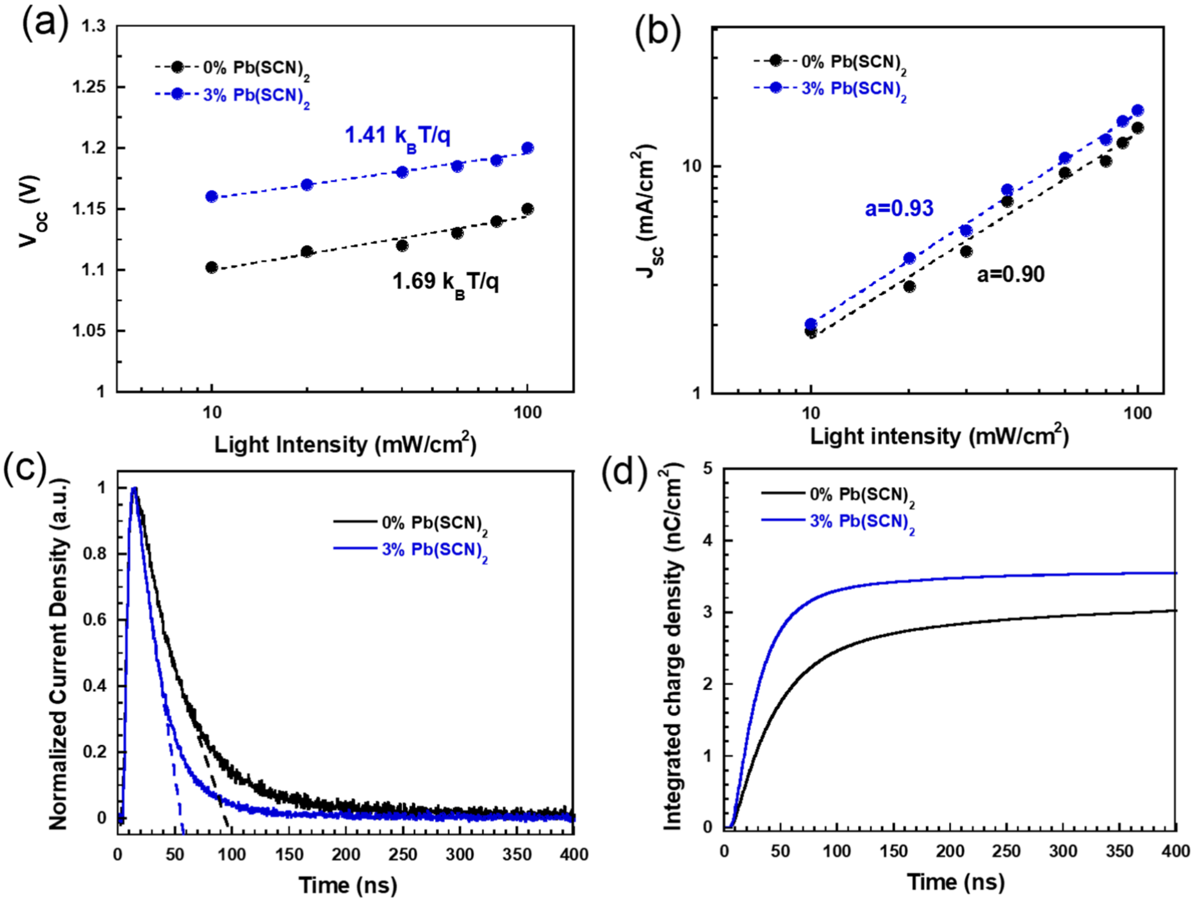

Figure 6. Light intensity dependence of (a) V_{OC} and (b) J_{SC} for PSCs with either the pristine quasi-2D $(PPA)_2(MA)_2Pb_3I_{10}$ thin film or the quasi-2D $(PPA)_2(MA)_2Pb_3I_{10}$ thin film processed with 3% $Pb(SCN)_2$ additives. (c) Normalized TPC curves and (d) integrated charge density curves of PSCs with either the pristine quasi-2D $(PPA)_2(MA)_2Pb_3I_{10}$ thin film or the quasi-2D $(PPA)_2(MA)_2Pb_3I_{10}$ thin film processed with 3% $Pb(SCN)_2$ additives, measured under −1 V applied bias at 590 nm wavelength.

Figure 5d shows the EQE spectra of PSCs. The PSCs with the quasi-2D $(PPA)_2(MA)_2Pb_3I_{10}$ thin film processed with 3% $Pb(SCN)_2$ additives possess higher EQE values than those with the pristine quasi-2D $(PPA)_2(MA)_2Pb_3I_{10}$ thin film. Based on the EQE spectra, the integrated photocurrent densities are 13.61 and 16.46 mA/cm^2 for PSCs with the pristine quasi-2D $(PPA)_2(MA)_2Pb_3I_{10}$ thin film and PSCs with the quasi-2D $(PPA)_2(MA)_2Pb_3I_{10}$ thin film processed with 3% $Pb(SCN)_2$ additives, respectively. The photocurrent densities obtained from the EQE spectra are consistent with J_{SC} values obtained from the J−V characteristics (Figure 5c). All these results demonstrate that $Pb(SCN)_2$ processing additives could effectively affect the electronic properties of quasi-2D $(PPA)_2(MA)_2Pb_3I_{10}$ thin films.

To understand the underlying physics of enlarged J_{SC} from PSCs with the quasi-2D $(PPA)_2(MA)_2Pb_3I_{10}$ thin film processed with 3% $Pb(SCN)_2$ additives, IS is utilized to investigate the charge-carrier transport and recombination processes within PSCs.[35] Under 1 sun illumination at the voltage of V_{OC}, the charge transfer resistance (R_{CT}) of PSCs with the pristine quasi-2D $(PPA)_2(MA)_2Pb_3I_{10}$ thin film is calculated to be ∼281 Ω, whereas an R_{CT} of ∼235 Ω is obtained for PSCs with the quasi-2D $(PPA)_2(MA)_2Pb_3I_{10}$ thin film processed with 3% $Pb(SCN)_2$ additives. A small R_{CT} indicates that PSCs exhibit a large J_{SC} (Supporting Information 2).[36] Thus, compared with PSCs with the pristine quasi-2D $(PPA)_2(MA)_2Pb_3I_{10}$ thin film, PSCs with the quasi-2D $(PPA)_2(MA)_2Pb_3I_{10}$ thin film processed with 3% $Pb(SCN)_2$ additives exhibit higher J_{SC}.

The charge-carrier recombination resistance (R_{rec}) values are further calculated from the IS spectra at low frequency measured in the dark (Supporting Information 2). The R_{rec} values of PSCs with the pristine quasi-2D $(PPA)_2(MA)_2Pb_3I_{10}$ thin film and PSCs with the quasi-2D $(PPA)_2(MA)_2Pb_3I_{10}$ thin film processed with 3% $Pb(SCN)_2$ additives are ∼5920, and ∼7500 Ω, respectively. Clearly, a higher R_{rec} indicates that a weaker charge-carrier recombination takes place in PSCs.[36] Thus, compared with PSCs with the pristine quasi-2D $(PPA)_2(MA)_2Pb_3I_{10}$ thin film, PSCs with the quasi-2D $(PPA)_2(MA)_2Pb_3I_{10}$ thin film processed with 3% $Pb(SCN)_2$ additives exhibit higher J_{SC}.

The light intensity dependence of V_{OC} is studied for further investigation charge-carrier recombination within PSCs.[37,38] V_{OC} correlated with the light intensity is described as $V_{OC} \propto S \ln(I)$, where $S = (nk_BT)/q$ (where k_B is the Boltzmann constant, q is the elementary charge, T is the room temperature in Kelvin, and I is the light intensity).[37] As $n \approx 1$, the bimolecular recombination is dominant in solar cells, while as $n \approx 2$, the monomolecular recombination is dominant in solar cells.[37] The light intensity dependence of V_{OC} for PSCs is shown in Figure 6a. Both PSCs follow the relationship of $V_{OC} \propto S \ln(I)$. For PSCs with the pristine quasi-2D $(PPA)_2(MA)_2Pb_3I_{10}$ thin film, $S = 1.69k_BT/q$, whereas for PSCs with the quasi-2D $(PPA)_2(MA)_2Pb_3I_{10}$ processed with

https://dx.doi.org/10.1021/acsami.0c16514
ACS Appl. Mater. Interfaces 2020, 12, 51744−51755

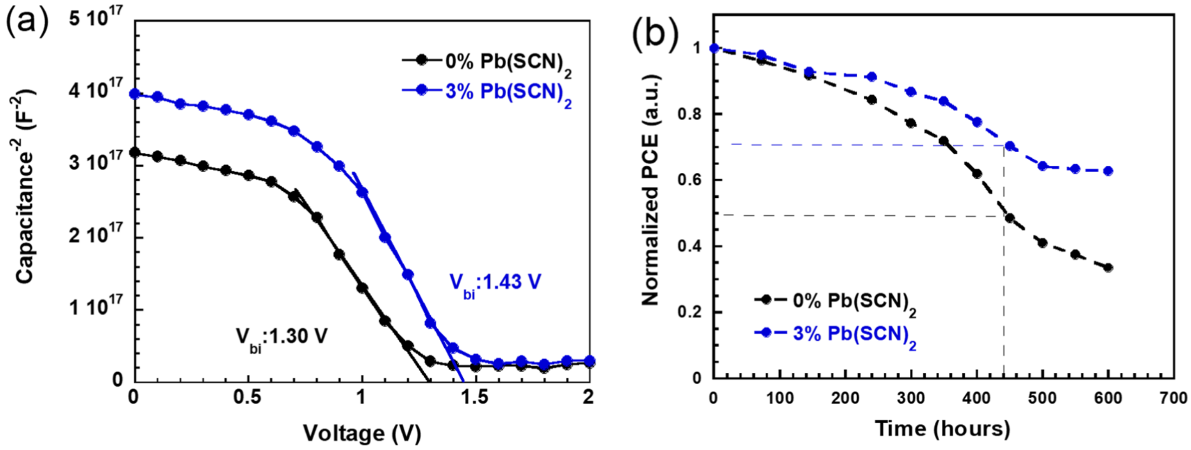

Figure 7. (a) Mott−Schottky analysis and (b) shelf stabilities of PSCs with either the pristine quasi-2D $(PPA)_2(MA)_2Pb_3I_{10}$ thin film or the quasi-2D $(PPA)_2(MA)_2Pb_3I_{10}$ thin film processed with 3% $Pb(SCN)_2$ additives.

3% $Pb(SCN)_2$ additives, $S = 1.41k_BT/q$. Thus, the monomolecular recombination is dominant in PSCs with the pristine quasi-2D $(PPA)_2(MA)_2Pb_3I_{10}$ thin film, whereas PSCs with the quasi-2D $(PPA)_2(MA)_2Pb_3I_{10}$ thin film processed with 3% $Pb(SCN)_2$ additives possess less monomolecular recombination. As a result, a higher J_{SC} is observed for PSCs with the quasi-2D $(PPA)_2(MA)_2Pb_3I_{10}$ thin film processed with 3% $Pb(SCN)_2$ additives.

The light intensity dependence of J_{SC} for PSCs is shown in Figure 6b. All PSCs exhibit a power-law dependence of J_{SC} on the light intensity, which is described as $J_{SC} \propto I^{\alpha}$ (where I is the light intensity and α is the coefficient).[37,38] As $\alpha = 1$, all charge carriers are swept out before recombination.[37,38] α values of 0.90 and 0.93 are observed from PSCs with the pristine quasi-2D $(PPA)_2(MA)_2Pb_3I_{10}$ thin film and PSCs with the quasi-2D $(PPA)_2(MA)_2Pb_3I_{10}$ thin film processed with 3% $Pb(SCN)_2$ additives, respectively. A larger α suggests that the bimolecular recombination is suppressed in PSCs with the quasi-2D $(PPA)_2(MA)_2Pb_3I_{10}$ thin film processed with 3% $Pb(SCN)_2$ additives. Thus, a larger J_{SC} is observed for PSCs with the quasi-2D $(PPA)_2(MA)_2Pb_3I_{10}$ thin film processed with 3% $Pb(SCN)_2$ additives.

TPC measurement is also carried out to investigate the charge-carrier extraction properties within PSCs. An external bias of −1 V is applied across PSCs to minimize the charge-carrier recombination.[21,22] Figure 6c presents the normalized photocurrent density curves, which are collected at a wavelength of 590 nm. The charge extraction time is estimated by extrapolating the normalized transient current density from the linear region to zero.[21,22] Charge-carrier extraction times of ∼100 ns and ∼60 ns are observed for PSCs with the pristine quasi-2D $(PPA)_2(MA)_2Pb_3I_{10}$ thin film and PSCs with the quasi-2D $(PPA)_2(MA)_2Pb_3I_{10}$ thin film processed with 3% $Pb(SCN)_2$ additives, respectively. A shorter charge-carrier extraction time indicates that an efficient charge extraction process takes place within PSCs. Moreover, as shown in Figure 6d, the significantly enlarged extracted charge-carrier densities are observed for PSCs with the quasi-2D $(PPA)_2(MA)_2Pb_3I_{10}$ thin film processed with 3% $Pb(SCN)_2$ additives, which indicates that more charge carriers are generated compared with those with the pristine quasi-2D $(PPA)_2(MA)_2Pb_3I_{10}$ thin film. All these results demonstrate that PSCs with the quasi-2D $(PPA)_2(MA)_2Pb_3I_{10}$ thin film processed with 3% $Pb(SCN)_2$ additives possess higher J_{SC} compared with those with the quasi-2D $(PPA)_2(MA)_2Pb_3I_{10}$ thin film.

The PL spectra of the $(PPA)_2(MA)_2Pb_3I_{10}$ thin film and quasi-2D $(PPA)_2(MA)_2Pb_3I_{10}$ thin film processed with 3% $Pb(SCN)_2$ additives coated on the glass substrates measured from both the front (air) side and the back (glass) side are investigated (Supporting Information 3). It is found that the shape of PL spectra for both two thin films is nearly identical, but the PL intensity of the quasi-2D $(PPA)_2(MA)_2Pb_3I_{10}$ thin film processed with 3% $Pb(SCN)_2$ additives is slightly higher than that of the $(PPA)_2(MA)_2Pb_3I_{10}$ thin film, which indicates that reduced nonradiative recombination takes place in the $(PPA)_2(MA)_2Pb_3I_{10}$ thin film processed with 3% $Pb(SCN)_2$ additives. These observations are consistent with the TIRFM results (Figure 4). In addition, an increased PL peak intensity, corresponding to the phase of $n = 5$ in the quasi-2D $(PPA)_2(MA)_2Pb_3I_{10}$ thin film processed with 3% $Pb(SCN)_2$ additives, from the back side is observed, which indicates that the distribution of n is indeed tuned by the addition of $Pb(SCN)_2$.

Mott−Schottky analysis, based on the $C-V$ measurement, is further carried out to investigate the built-in potentials (V_{bi}) of PSCs.[39,40] As shown in Figure 7a, under forward bias, the V_{bi} of PSCs is extracted from $C^{-2} = \frac{2(V_{bi} - V)}{q\varepsilon\varepsilon_0 A^2 n_{trap}}$[39,40] (where ε is the dielectric constant, ε_0 is the vacuum permittivity, and A is the active area) by extrapolating the linear fitting line to the intercept on the x-axis.[6] A V_{bi} of ∼1.43 V is observed for PSCs with the quasi-2D $(PPA)_2(MA)_2Pb_3I_{10}$ thin film processed with 3% $Pb(SCN)_2$ additives, whereas a V_{bi} of ∼1.30 V is observed for PSCs with the pristine quasi-2D $(PPA)_2(MA)_2Pb_3I_{10}$ thin film. Therefore, as expected, PSCs with the quasi-2D $(PPA)_2(MA)_2Pb_3I_{10}$ thin film processed with 3% $Pb(SCN)_2$ additives exhibit a larger V_{OC} compared to those with the pristine quasi-2D $(PPA)_2(MA)_2Pb_3I_{10}$ thin film.

The photocurrent hysteresis behaviors of PSCs are further studied. The $J-V$ characteristics of PSCs with either the pristine quasi-2D $(PPA)_2(MA)_2Pb_3I_{10}$ thin film or the quasi-2D $(PPA)_2(MA)_2Pb_3I_{10}$ thin film processed with 3% $Pb(SCN)_2$ additives under different scan directions with a scan rate of 0.05 V/s are presented in Supporting Information 4. The photocurrent hysteresis behaviors are described by the photocurrent hysteresis index (HI), which is defined as $HI = \frac{PCE_{reverse} - PCE_{forward}}{PCE_{reverse}}$,[41] where $PCE_{reverse}$ and $PCE_{forward}$ are

Table 2. Photocurrent Hysteresis Behaviors of PSCs with the Quasi-2D $(PPA)_2(MA)_2Pb_3I_{10}$ Thin Film

Quasi-2D $(PPA)_2(MA)_2Pb_3I_{10}$ thin film	scan[a] direction	J_{SC} (mA/cm^2)	V_{OC} (V)	FF (%)	PCE (%)	HI
processed without $Pb(SCN)_2$	forward	13.50	1.12	70	10.58	0.08
	reverse	14.12	1.15	71	11.52	
processed with 3% $Pb(SCN)_2$	forward	16.67	1.19	72	14.32	0.04
	reverse	17.25	1.20	72	14.90	

[a]The scan rate is 0.05 V/s.

PCEs observed from the reverse and forward scan directions, respectively. The HI values of PSCs are summarized in Table 2. The PSCs fabricated with the pristine quasi-2D $(PPA)_2(MA)_2Pb_3I_{10}$ thin film possess an HI of 0.08, whereas the PSCs fabricated with the quasi-2D $(PPA)_2(MA)_2Pb_3I_{10}$ thin film processed with 3% $Pb(SCN)_2$ additives possess an HI of 0.04. Such suppressed hysteresis is attributed to the reduced grain boundary in the quasi-2D $(PPA)_2(MA)_2Pb_3I_{10}$ thin film processed with 3% $Pb(SCN)_2$ additive.[3]

The shelf stabilities of unencapsulated PSCs stored in a glovebox with a nitrogen atmosphere are shown in Figure 7b. PSCs with the quasi-2D $(PPA)_2(MA)_2Pb_3I_{10}$ thin film processed with 3% $Pb(SCN)_2$ additives retain 60% of their initial PCEs after 600 h, whereas PSCs with the pristine quasi-2D $(PPA)_2(MA)_2Pb_3I_{10}$ thin film show a degradation after 150 h and degrade more than 50% of their original PCEs after 450 h. Note that PSCs with quasi-2D $(PPA)_2(MA)_2Pb_3I_{10}$ thin films possess better stability than those with the 3D $MAPbI_3$ thin film.[42,43] The enhanced stability of PSCs is attributed to the hydrophobic nature and the pinhole-free quasi-2D $(PPA)_2(MA)_2Pb_3I_{10}$ thin film processed with 3% $Pb(SCN)_2$ additives. Unfortunately, both PSCs have a faster degradation at both room temperature and high temperature (Supporting Information 5) compared to those with 2D perovskites with either the Dion−Jacobson phase or alternative cation in the interlayer space phase.[17,19,20,44,45]

CONCLUSIONS

In conclusion, we have developed novel quasi-2D $(PPA)_2(MA)_2Pb_3I_{10}$ thin films, where PPA with carbon−carbon triple bond (C≡C) and shorter chain length was employed to form a quasi-2D perovskite structure. PSCs with a pristine quasi-2D $(PPA)_2(MA)_2Pb_3I_{10}$ thin film exhibited a PCE of 12.16%. To further boost PCEs of PSCs with the quasi-2D $(PPA)_2(MA)_2Pb_3I_{10}$ thin film, quasi-2D $(PPA)_2(MA)_2Pb_3I_{10}$ thin films were processed with $Pb(SCN)_2$ additives. Systematical studies indicated that the quasi-2D $(PPA)_2(MA)_2Pb_3I_{10}$ thin film processed with $Pb(SCN)_2$ additives possesses larger crystals, superior film morphology, reduced nonradiative recombination, and enhanced and balanced charge-carrier mobilities. As a result, the PSC with the quasi-2D $(PPA)_2(MA)_2Pb_3I_{10}$ thin film processed with $Pb(SCN)_2$ additives affords a PCE of 15.20% and dramatically suppressed photocurrent hysteresis. Moreover, PSCs with the quasi-2D $(PPA)_2(MA)_2Pb_3I_{10}$ thin films processed with $Pb(SCN)_2$ additives exhibited boosted stability compared to those with pristine quasi-2D $(PPA)_2(MA)_2Pb_3I_{10}$ thin films. All these results demonstrated that we provided an effective approach to realize stable and efficient PSCs with 2D perovskite materials.

ASSOCIATED CONTENT

Supporting Information

The Supporting Information is available free of charge at https://pubs.acs.org/doi/10.1021/acsami.0c16514.

TIRFM images of perovskite particles, charge transport properties, PL spectra, photocurrent hysteresis, and thermal stability test (PDF)

AUTHOR INFORMATION

Corresponding Author

Xiong Gong − *School of Polymer Science and Polymer Engineering, The University of Akron, Akron, Ohio 44325, United States;* orcid.org/0000-0001-6525-3824; Email: xgong@uakron.edu; Fax: (330) 9723406

Authors

Tao Zhu − *School of Polymer Science and Polymer Engineering, The University of Akron, Akron, Ohio 44325, United States*

Yongrui Yang − *School of Polymer Science and Polymer Engineering, The University of Akron, Akron, Ohio 44325, United States*

Kai Gu − *School of Polymer Science and Polymer Engineering, The University of Akron, Akron, Ohio 44325, United States*

Chunming Liu − *School of Polymer Science and Polymer Engineering, The University of Akron, Akron, Ohio 44325, United States*

Jie Zheng − *Department of Chemical and Biomolecular Engineering, College of Engineering and Polymer Science, The University of Akron, Akron, Ohio 44325, United States;* orcid.org/0000-0003-1547-3612

Complete contact information is available at: https://pubs.acs.org/10.1021/acsami.0c16514

Notes

The authors declare no competing financial interest.

ACKNOWLEDGMENTS

The authors acknowledge the National Science Foundation (ECCS/EPMD1903303) and Air Force Office of Scientific Research (AFOSR) (through the Organic Materials Chemistry Program, grant number: FA9550-15-1-0292, Program Manager, Dr. Kenneth Caster) for financial support.

REFERENCES

(1) Kojima, A.; Teshima, K.; Shirai, Y.; Miyasaka, T. Organometal Halide Perovskites as Visible-Light Sensitizers for Photovoltaic Cells. *J. Am. Chem. Soc.* **2009**, *131*, 6050−6051.

(2) Wehrenfennig, C.; Eperon, G. E.; Johnston, M. B.; Snaith, H. J.; Herz, L. M. High Charge Carrier Mobilities and Lifetimes in Organolead Trihalide Perovskites. *Adv. Mater.* **2014**, *26*, 1584−1589.

(3) Shi, D.; Adinolfi, V.; Comin, R.; Yuan, M.; Alarousu, E.; Buin, A.; Chen, Y.; Hoogland, S.; Rothenberger, A.; Katsiev, K.; Losovyj, Y.; Zhang, X.; Dowben, P. A.; Mohammed, O. F.; Sargent, E. H.; Bakr, O.

M. Low Trap-State Density and Long Carrier Diffusion in Organolead Trihalide Perovskite Single Crystals. *Science* **2015**, *347*, 519−522.

(4) Kumar, G. R.; Savariraj, A. D.; Karthick, S. N.; Selvam, S.; Balamuralitharan, B.; Kim, H. J.; Viswanathan, K. K.; Vijaykumar, M.; Prabakar, K. Phase Transition Kinetics and Surface Binding States of Methylammonium Lead Iodide Perovskite. *Phys. Chem. Chem. Phys.* **2016**, *18*, 7284−7292.

(5) Xu, W.; Zheng, L.; Zhang, X.; Cao, Y.; Meng, T.; Wu, D.; Liu, L.; Hu, W.; Gong, X. Efficient Perovskite Solar Cells Fabricated by Co Partially Substituted Hybrid Perovskite. *Adv. Energy Mater.* **2018**, *8*, 1703178.

(6) Wang, K.; Zheng, L.; Zhu, T.; Yao, X.; Yi, C.; Zhang, X.; Cao, Y.; Liu, L.; Hu, W.; Gong, X. Efficient Perovskite Solar Cells by Hybrid Perovskites Incorporated with Heterovalent Neodymium Cations. *Nano Energy* **2019**, *61*, 352−360.

(7) NREL Efficiency Chart Vol. 2019, https://www.nrel.gov/pv/assets/pdfs/best-reserch-cell-efficiencies.20190802.pdf (accessed August, 2019).

(8) Wang, K.; Zheng, L.; Zhu, T.; Liu, L.; Becker, M. L.; Gong, X. High Performance Perovskites Solar Cells by Hybrid Perovskites Co-Crystallized with Poly (Ethylene Oxide). *Nano Energy* **2020**, *67*, 104229.

(9) Mao, L.; Stoumpos, C. C.; Kanatzidis, M. G. Two-Dimensional Hybrid Halide Perovskites: Principles and Promises. *J. Am. Chem. Soc.* **2018**, *141*, 1171−1190.

(10) Mao, L.; Ke, W.; Pedesseau, L.; Wu, Y.; Katan, C.; Even, J.; Wasielewski, M. R.; Stoumpos, C. C.; Kanatzidis, M. G. Hybrid Dion-Jacobson 2D Lead Iodide Perovskites. *J. Am. Chem. Soc.* **2018**, *140*, 3775−3783.

(11) Zhou, N.; Huang, B.; Sun, M.; Zhang, Y.; Li, L.; Lun, Y.; Wang, X.; Hong, J.; Chen, Q.; Zhou, H. The Spacer Cations Interplay for Efficient and Stable Layered 2D Perovskite Solar Cells. *Adv. Energy Mater.* **2020**, *10*, 1901566.

(12) Zhang, Y.; Chen, J.; Lian, X.; Qin, M.; Li, J.; Andersen, T. R.; Lu, X.; Wu, G.; Li, H.; Chen, H. Highly Efficient Guanidinium-Based Quasi 2D Perovskite Solar Cells via a Two-Step Post-Treatment Process. *Small Methods* **2019**, *3*, 1900375.

(13) Cao, D. H.; Stoumpos, C. C.; Farha, O. K.; Hupp, J. T.; Kanatzidis, M. G. 2D Homologous Perovskites as Light-Absorbing Materials for Solar Cell Applications. *J. Am. Chem. Soc.* **2015**, *137*, 7843−7850.

(14) Qiu, J.; Xia, Y.; Zheng, Y.; Hui, W.; Gu, H.; Chou, L. 2D Intermediate Suppression for Efficient Ruddlesden-Popper (RP) Phase Lead-Free Perovskite Solar Cells. *ACS Energy Lett.* **2019**, *4*, 1513−1520.

(15) Zhang, F.; Kim, D. H.; Lu, H.; Park, J.-S.; Larson, B. W.; Hu, J.; Gao, L.; Xiao, C.; Reid, O. G.; Chen, X.; Zhao, Q.; Ndione, P. F.; Berry, J. J.; You, W.; Walsh, A.; Beard, M. C.; Zhu, K. Enhanced Charge Transport in 2D Perovskites via Fluorination of Organic Cation. *J. Am. Chem. Soc.* **2019**, *141*, 5972−5979.

(16) Wang, K.; Wu, C.; Jiang, Y.; Yang, D.; Wang, K.; Priya, S. Distinct Conducting Layer Edge States in Two-Dimensional (2D) Halide Perovskite. *Sci. Adv.* **2019**, *5*, No. eaau3241.

(17) Li, P.; Liang, C.; Liu, X. L.; Li, F.; Zhang, Y.; Liu, X. T.; Gu, H.; Hu, X.; Xing, G.; Tao, X.; Song, Y. Low-Dimensional Perovskites with Diammonium and Monoammonium Alternant Cations for High-Performance Photovoltaics. *Adv. Mater.* **2019**, *31*, 1901966.

(18) Xu, Z.; Lu, D.; Liu, F.; Lai, H.; Wan, X.; Zhang, X.; Liu, Y.; Chen, Y. Phase Distribution and Carrier Dynamics in Multiple-Ring Aromatic Spacer-Based Two-Dimensional Ruddlesden-Popper Perovskite Solar Cells. *ACS Nano* **2020**, *14*, 4871−4881.

(19) Lai, H.; Lu, D.; Xu, Z.; Zheng, N.; Xie, Z.; Liu, Y. Organic-Salt-Assisted Crystal Growth and Orientation of Quasi-2D Ruddlesden-Popper Perovskites for Solar Cells with Efficiency over 19%. *Adv. Mater.* **2020**, *32*, 2001470.

(20) Luo, T.; Zhang, Y. L.; Xu, Z.; Niu, T. Q.; Wen, J. L.; Lu, J.; Jin, S. Y.; Liu, S. Z.; Zhao, K. Compositional Control in 2D Perovskites with Alternating Cations in the Interlayer Space for Photovoltaics with Efficiency over 18%. *Adv. Mater.* **2019**, *31*, 1903848.

(21) Zhu, T.; Zheng, L.; Xiao, Z.; Meng, X.; Liu, L.; Ding, L.; Gong, X. Functionality of Non-Fullerene Electron Acceptors in Ternary Organic Solar Cells. *Sol. RRL* **2019**, *3*, 1900322.

(22) Seifter, J.; Sun, Y.; Heeger, A. J. Transient Photocurrent Response of Small-Molecule Bulk Heterojunction Solar Cells. *Adv. Mater.* **2014**, *26*, 2486−2493.

(23) Kitazawa, N. Optical Absorption and Photoluminescence Properties of Pb(I, Br)-Based Two-Dimensional Layered Perovskite. *Jpn. J. Appl. Phys.* **1997**, *36*, 2272.

(24) Kim, H.; Lee, Y. H.; Lyu, T.; Yoo, J. H.; Park, T.; Oh, J. H. Boosting the Performance and Stability of Quasi-Two-Dimensional Tin-Based Perovskite Solar Cells using the Formamidinium Thiocyanate Additive. *J. Mater. Chem. A* **2018**, *6*, 18173−18182.

(25) Jin, S.; Wei, Y.; Yang, X.; Luo, D.; Fang, Y.; Zhao, Y.; Guo, Q.; Huang, Y.; Fan, L.; Wu, J. Additive Engineering Induced Perovskite Crystal Growth for High Performance Perovskite Solar Cells. *Org. Electron.* **2018**, *63*, 207−215.

(26) Pecharsky, V.; Zavalij, P. *Fundamentals of Powder Diffraction and Structural Characterization of Materials*; Springer Science & Business Media, 2008.

(27) Zheng, L.; Wang, K.; Zhu, T.; Yang, Y.; Chen, R.; Gu, K.; Liu, C.; Gong, X. High-Performance Perovskite Solar Cells by One-Step Self-Assembled Perovskite-Polymer Thin Films. *ACS Appl. Energy Mater.* **2020**, *3*, 5902−5912.

(28) Bube, R. H. Trap Density Determination by Space-Charge-Limited Currents. *J. Appl. Phys.* **1962**, *33*, 1733−1737.

(29) Duijnstee, E. A.; Ball, J. M.; Le Corre, V. M.; Koster, L. J. A.; Snaith, H. J.; Lim, J. Toward Understanding Space-Charge Limited Current Measurements on Metal Halide Perovskites. *ACS Energy Lett.* **2020**, *5*, 376−384.

(30) Zhang, X.; Ren, X.; Liu, B.; Munir, R.; Zhu, X.; Yang, D.; Li, J.; Liu, Y.; Smilgies, D.-M.; Li, R.; Yang, Z.; Niu, T.; Wang, X.; Amassian, A.; Zhao, K.; Liu, S. Stable High Efficiency Two-Dimensional Perovskite Solar Cells via Cesium Doping. *Energy Environ. Sci.* **2017**, *10*, 2095−2102.

(31) Dong, Q.; Fang, Y.; Shao, Y.; Mulligan, P.; Qiu, J.; Cao, L.; Huang, J. Electron-Hole Diffusion Lengths > 175 μm in Solution-Grown $CH_3NH_3PbI_3$ Single Crystals. *Science* **2015**, *347*, 967−970.

(32) Lin, Y.; Fang, Y.; Zhao, J.; Shao, Y.; Stuard, S. J.; Nahid, M. M.; Ade, H.; Wang, Q.; Shield, J. E.; Zhou, N.; Moran, A. M.; Huang, J. Unveiling the Operation Mechanism of Layered Perovskite Solar Cells. *Nat. Commun.* **2019**, *10*, 1008.

(33) Zhang, X.; Wu, G.; Fu, W.; Qin, M.; Yang, W.; Yan, J.; Zhang, Z.; Lu, X.; Chen, H. Orientation Regulation of Phenylethylammonium Cation based 2D Perovskite Solar Cell with Efficiency Higher than 11%. *Adv. Energy Mater.* **2018**, *8*, 1702498.

(34) Zhang, H.; Hou, M.; Xia, Y.; Wei, Q.; Wang, Z.; Cheng, Y.; Chen, Y.; Huang, W. Synergistic Effect of Anions and Cations in Additives for Highly Efficient and Stable Perovskite Solar Cells. *J. Mater. Chem. A* **2018**, *6*, 9264−9270.

(35) Xu, W.; Zheng, L.; Zhu, T.; Liu, L.; Gong, X. Bulk Heterojunction Perovskite Solar Cells Incorporated with Zn_2SnO_4 Nanoparticles as the Electron Acceptors. *ACS Appl. Mater. Interfaces* **2019**, *11*, 34020−34029.

(36) Fabregat-Santiago, F.; Garcia-Belmonte, G.; Mora-Seró, I.; Bisquert, J. Characterization of Nanostructured Hybrid and Organic Solar Cells by Impedance Spectroscopy. *Phys. Chem. Chem. Phys.* **2011**, *13*, 9083−9118.

(37) Cowan, S. R.; Banerji, N.; Leong, W. L.; Heeger, A. J. Charge Formation, Recombination, and Sweep-Out Dynamics in Organic Solar Cells. *Adv. Funct. Mater.* **2012**, *22*, 1116−1128.

(38) Cowan, S. R.; Roy, A.; Heeger, A. J. Recombination in Polymer-Fullerene Bulk Heterojunction Solar Cells. *Phys. Rev. B: Condens. Matter Mater. Phys.* **2010**, *82*, 245207.

(39) Mingebach, M.; Deibel, C.; Dyakonov, V. Built-in Potential and Validity of the Mott-Schottky Analysis in Organic Bulk Heterojunction Solar Cells. *Phys. Rev. B: Condens. Matter Mater. Phys.* **2011**, *84*, 153201.

https://dx.doi.org/10.1021/acsami.0c16514
ACS Appl. Mater. Interfaces 2020, 12, 51744−51755

(40) Murgatroyd, P. N. Theory of Space-Charge-Limited Current Enhanced by Frenkel Effect. *J. Phys. D: Appl. Phys.* **1970**, *3*, 151.
(41) Kim, H.-S.; Park, N.-G. Parameters Affecting I-V Hysteresis of $CH_3NH_3PbI_3$ Perovskite Solar Cells: Effects of Perovskite Crystal Size and Mesoporous TiO_2 Layer. *J. Phys. Chem. Lett.* **2014**, *5*, 2927−2934.
(42) Zheng, L.; Mukherjee, S.; Wang, K.; Hay, M. E.; Boudouris, B. W.; Gong, X. Radical Polymers as Interfacial Layers in Inverted Hybrid Perovskite Solar Cells. *J. Mater. Chem. A* **2017**, *5*, 23831.
(43) Zhou, S.; Zhu, T.; Zheng, L.; Zhang, D.; Xu, W.; Liu, L.; Cheng, G.; Zheng, J.; Gong, X. A Zwitterionic Polymer as an Interfacial Layer for Efficient and Stable Perovskite Solar Cells. *RSC Adv.* **2019**, *9*, 30317.
(44) Ahmad, S.; Fu, P.; Yu, S.; Yang, Q.; Liu, X.; Wang, X.; Wang, X.; Guo, X.; Li, C. Dion-Jacobson Phase 2D Layered Perovskites for Solar Cells with Ultrahigh Stability. *Joule* **2019**, *3*, 794−806.
(45) Li, Y.; Milić, J. V.; Ummadisingu, A.; Seo, J.-Y.; Im, J.-H.; Kim, H.-S.; Liu, Y.; Dar, M. I.; Zakeeruddin, S. M.; Wang, P.; Hagfeldt, A.; Grätzel, M. Bifunctional Organic Spacers for Formamidinium-Based Hybrid Dion-Jacobson Two-Dimensional Perovskite Solar Cells. *Nano Lett.* **2019**, *19*, 150−157.

https://dx.doi.org/10.1021/acsami.0c16514
ACS Appl. Mater. Interfaces 2020, 12, 51744−51755